ANALYTICAL SOLUTIONS FOR MARTIAN NIGHTTIME OH* LAYER

M. Grygalashvyly, *Max Planck Institute for Solar System Research, Göttingen, Germany (gryga@iap-kborn.de)*, **D. S. Shaposhnikov,** *Moscow Institute of Physics and Technology, Moscow, Russia*, **A. S. Medvedev,** *Max Planck Institute for Solar System Research, Göttingen, Germany*, **G. R. Sonnemann,** *Max Planck Institute for Solar System Research, Göttingen, Germany*, **P. Hartogh,** *Max Planck Institute for Solar System Research, Göttingen, Germany.*

Introduction:

Airglow emissions of OH* in the Earth mesopause region are used for obtaining information about gravity wave, planetary wave and tidal parameters, chemical distributions (O and H), and temperature (trends, solar cycle effects, and annual variations). Recently, hydroxyl emissions were found in the Martian atmosphere (Clancy et al., 2013), thus, we can expect similar applications of this emission for this planet.

In order to study morphology and variability of the layer, the corresponding parameters should be introduced. The concentration of OH* at peak and peak altitude represent a natural choice for this purpose. For interpretation of measurements, it is desirable to establish straightforward relations between these quantities and the ambient temperature, air density and concentration of minor species involved in photochemical reactions.

Analytical Approaches:

Assuming the photochemical equilibrium for excited hydroxyl in the vicinity of OH* layer (~40-60 km) at nighttime conditions (García-Muñoz et al., 2005) and omitting the reaction HO_2 with O as negligible for population of OH* (Xu et al., 2012; García-Muñoz et al., 2005), we start from the almost full equation for vibrationally exited hydroxyl:

$$[OH_v] \approx$$

$$\frac{\left(\begin{array}{c} f_v r_1[H][O_3] + \sum_{v'=v+1}^{9} A_{v'v}[OH_{v'}][CO_2] + \\ \sum_{v'=v+1}^{9} G_{v'v}[OH_{v'}][N_2] + \sum_{v'=v+1}^{9} B_{v'v}[OH_{v'}][O_2] \\ + \sum_{v'=v+1}^{9} D_{v'v}[OH_{v'}][O] + \sum_{v'=v+1}^{9} E_{v'v}[OH_{v'}] \end{array}\right)}{\left(\begin{array}{c} \sum_{v''=0}^{v-1} A_{vv''}[CO_2] + \sum_{v''=0}^{v-1} G_{vv''}[N_2] + \\ \sum_{v''=0}^{v-1} B_{vv''}[O_2] + \sum_{v''=0}^{v-1} D_{vv''}[O] + \sum_{v''=0}^{v-1} E_{vv''} + \\ + r_4(v)[O] \end{array}\right)}, \quad (1)$$

where v is vibrational number (here and after $v < v'$; $v'' < v$); f_v is the nascent distributions, r – reaction rates, A, B, G, and D are the quenching coefficients for CO_2, O_2, N_2, and O, respectively. All used reactions and processes are collected in Table 1. Hereafter, the square brackets denote number density of the given chemical constituents.

Considering only main processes of production and relaxation (reaction of O_3 with H, quenching by CO_2, O_2, and N_2), we can simplify Eq. (1):

$$[OH_v] \approx$$

$$\left(\begin{array}{c} f_v r_1[H][O_3] + \sum_{v'=v+1}^{9} A_{v'v}[OH_{v'}][CO_2] + \\ \sum_{v'=v+1}^{9} B_{v'v}[OH_{v'}][O_2] + \sum_{v'=v+1}^{9} G_{v'v}[OH_{v'}][N_2] \end{array}\right) \Big/ \left(\begin{array}{c} \sum_{v''=0}^{v-1} A_{vv''}[CO_2] + \sum_{v''=0}^{v-1} B_{vv''}[O_2] + \\ + \sum_{v''=0}^{v-1} G_{vv''}[N_2] \end{array}\right) \cdot (2)$$

We omitted spontaneous emission and quenching by O as much weaker processes. Indeed, for $OH_{v=9}$ and $OH_{v=1}$ the total spontaneous emission coefficients amount to $E_9 = 199.3$ s^{-1} and $E_1 = 17.6$ s^{-1} (Xu et al., 2012), respectively. On the other hand, for example at 50 km, $[CO_2] \geq 10^{15}$ cm^{-3} (e.g. Krasnopolsky and Lefèvre, 2013), total collisional removal rates $A_9 = 9.1 \cdot 10^{-11}$ $cm^3 s^{-1}$ and $A_1 = 2.9 \cdot 10^{-13}$ $cm^3 s^{-1}$ (e.g. Krasnopolsky (2013), García-Muñoz et al. (2005)), therefore the first term in the denominator of Eq. (1) for corresponding vibrational numbers amounts to $\geq 9 \cdot 10^4$ s^{-1} and $\geq 2.9 \cdot 10^2$ s^{-1}, respectively. [O] at 50-60 km is ~10^9-10^{11} cm^{-3} (e.g. Krasnopolsky and Lefèvre, 2013; Krasnopolsky, 2010; Krasnopolsky, 2006). Caridade et al. (2013) derives total values for reactive ($O + OH_v \rightarrow O_2 + H$) and non-reactive ($O + OH_v \rightarrow OH_{v'<v} + O$) quenching rates by O at temperature 160 K as $7.7 \cdot 10^{-11}$ $cm^3 s^{-1}$ and $6 \cdot 10^{-11}$ $cm^3 s^{-1}$ for vibrational numbers nine and one, respectively. Hence, the corresponding collisional removal due to atomic oxygen ≤ 8-6 s^{-1} for all vibrational numbers, and can be safely neglected.

Table 1. List and nomenclature of reaction rates, quenching coefficients, spontaneous emission coefficients (references: [1,2,3]Burkholder et al. (2020), [1,5]Adler-Golden (1997), [4,5]Caridade et al. (2013), [5]Makhlouf et al. (1995), [5]Krasnopolsky (2013), [6]Xu et al. (2012)).

	Reactions	Coefficients
1	$H + O_3$ $\xrightarrow{f_v r_1} OH_{v=5,...,9} + O_2$	$r_1 = 1.4 \cdot 10^{-10} exp\left(\frac{-470}{T}\right)$ $f_{v=9,...,5}$ $= 0.47, 0.34, 0.15, 0.03, 0.01$
2	$O + O_2 + CO_2$ $\rightarrow O_3 + CO_2$	$r_2 = 6.1 \cdot 10^{-34}(298/T)^{2.4}$
3	$O + O_3 \rightarrow 2O_2$	$r_3 = 8 \cdot 10^{-12} exp\left(\frac{-2060}{T}\right)$
4	$O + OH_{v=1,..,9} \rightarrow O_2$ $+ H$	$r_4(v = 9, ..., 1) = (5.42, 4.8,$ $4.42, 4, 3.77, 4.43, 3.74, 3, 3.15)$ $\cdot 10^{-11}$
5	OH_v $+ CO_2, O_2, N_2, O$ $\rightarrow OH_{v'<v} + CO_2$	$A_{vv'}, B_{vv'}, G_{vv'}, D_{vv'}$ See text
6	OH_v $\rightarrow OH_{v'<v} + hv$	$E_{vv'}$

Following García-Muñoz et al. (2005), we assume O_3 in the photochemical equilibrium in the vicinity of nighttime OH* layer. Then the ozone balance

equation for nighttime conditions can be represented as follows:

$$r_2[O][O_2][CO_2] = r_1[O_3][H] + r_3[O][O_3]. \quad (3)$$

The share of the reaction of O_3 with O in total ozone loss is small, since for typical temperatures at 50-60 km (~150 K) r_3 (~$8.7 \cdot 10^{-18}$ cm^{3}s^{-1}) is ~10^6 times smaller than r_1 (~$6.1 \cdot 10^{-12}$ cm^{3}s^{-1}), but [H] smaller than [O] no more than ~10^2-10^3 times in this region (García-Muñoz et al., 2005; Krasnopolsky, 2006; Krasnopolsky and Lefèvre, 2013). Thus, the second term in the right-hand side of Eq. (3) can be omitted and it becomes

$$r_2[O][O_2][CO_2] \approx r_1[O_3][H]. \quad (4)$$

Substituting Eq. (4) into the first term in the numerator of Eq. (2) we obtain

$$[OH_v] \approx$$
$$\frac{\left(\begin{array}{c} f_v r_2[O][O_2][CO_2] + \sum_{v'=v+1}^{9} A_{v'v}[OH_{v'}][CO_2] + \\ \sum_{v'=v+1}^{9} B_{v'v}[OH_{v'}][O_2] + \sum_{v'=v+1}^{9} G_{v'v}[OH_{v'}][N_2] \end{array} \right)}{\sum_{v''=0}^{v-1} A_{vv''}[CO_2] + \sum_{v''=0}^{v-1} B_{vv''}[O_2] + \sum_{v''=0}^{v-1} G_{vv''}[N_2]}. \quad (5)$$

Taking into account the linear proportionality of the molecular oxygen and molecular nitrogen number densities to the carbon dioxide and to the concentration of air ($[O_2] = \alpha[CO_2] = \beta M$, $[N_2] = \chi[CO_2]$) in the vicinity of OH* layer (e.g. Krasnopolsky, 2010; Krasnopolsky and Lefèvre, 2013), Eq. (5) can be rearranged as follows:

$$[OH_v] \approx \frac{\beta f_v r_2[O]M + [OH_{v'}]\sum_{v'=v+1}^{9} C_{v'v}}{\sum_{v''=0}^{v-1} C_{vv''}}, \quad (6)$$

where $\sum_{v'=v+1}^{9} C_{v'v} = \sum_{v'=v+1}^{9} A_{v'v} + \alpha \sum_{v'=v+1}^{9} B_{v'v} + \chi \sum_{v'=v+1}^{9} G_{v'v}$ and $\sum_{v''=0}^{v-1} C_{vv''} = \sum_{v''=0}^{v-1} A_{vv''} + \alpha \sum_{v''=0}^{v-1} B_{vv''} + \chi \sum_{v''=0}^{v-1} G_{vv''}$.

Writing reaction rate r_2 explicitly and reorganizing Eq. (6), we obtain:

$$[OH_v] \approx \varepsilon \gamma_v[O]T^{-2.4}M, \quad (7)$$

where $\varepsilon = 6.1 \cdot 10^{-24} \cdot 298^{2.4}\beta$ and $\gamma_v = \frac{f_v + \sum_{v'=v+1}^{v'=9} \gamma_{v'} C_{v'v}}{\sum_{v''=0}^{v''=v-1} C_{vv''}}$, $(f_{9<v<5} = 0)$. Note that the numerical coefficient in ε, which comes from the reaction rate r_2, can be different. Nevertheless, all studies are in consensus that $r_2 \sim T^{-2.4}$.

Peak altitude. Eq. (7) can be rewritten applying the ideal gas law:

$$[OH_v] \approx \vartheta_v T^{-3.4}[O]p, \quad (8)$$

where $\vartheta_v = \varepsilon \gamma_v/k_b$, k_b is Boltzmann constant, and p is pressure.

Differentiating by pressure and equating to zero, we derive the expression for pressure at local maximum of the excited hydroxyl concentration:

$$p_{max} \approx \frac{1}{3.4 \frac{\partial \ln T}{\partial p} - \frac{\partial \ln[O]}{\partial p}} \approx 1 \bigg/ \frac{\partial}{\partial p}\left(\ln\left(\frac{T^{3.4}}{[O]}\right)\right)', \quad (9)$$

Substituting (9) into (8), we obtain the expression for excited hydroxyl at their maximum:

$$[OH_v]_{max} \approx \frac{\vartheta_v T^{-3.4}[O]}{3.4 \frac{\partial \ln T}{\partial p} - \frac{\partial \ln[O]}{\partial p}} \approx \frac{\vartheta_v T^{-3.4}[O]}{\frac{\partial}{\partial p}\left(\ln\left(\frac{T^{3.4}}{[O]}\right)\right)}. \quad (10)$$

Relative variations. Decomposing in Eq. (7) [O], temperature, and air number density the averaged ($\overline{[O]}$, $\overline{T}$, $\overline{M}$) and variable parts ($[O]'$, T', M') yields

$$[OH_v] \approx \varepsilon \gamma_v (\overline{[O]} + [O]')(\overline{T} + T')^{-2.4}(\overline{[M]} + [M]'). \quad (11)$$

In Eq. (11), we apply the Taylor expansion to the term with temperature and cross-multiply all terms:

$$[OH_v] \approx \varepsilon \gamma_v \overline{[O]}\,\overline{T}^{-2.4}\overline{[M]} + \varepsilon \gamma_v \overline{[O]}\,\overline{T}^{-2.4}[M]' + \varepsilon \gamma_v[O]'\overline{T}^{-2.4}\overline{[M]} - 2.4\varepsilon \gamma_v \overline{[O]}T'\overline{T}^{-3.4}\overline{[M]} + \varepsilon \gamma_v[O]'\overline{T}^{-2.4}[M]' - 2.4\varepsilon \gamma_v \overline{[O]}T'\overline{T}^{-3.4}[M]' - 2.4\varepsilon \gamma_v[O]'T'\overline{T}^{-3.4}\overline{[M]} - 2.4\varepsilon \gamma_v[O]'T'\overline{T}^{-3.4}[M]'. \quad (12)$$

The exited hydroxyl concentration for a given vibrational number can be written as follows:

$$[OH_v] \approx \overline{[OH_v]} + [OH_v]'_M + [OH_v]'_O + [OH_v]'_T + [OH_v]''_{OM} + [OH_v]''_{TM} + [OH_v]''_{TO} + hi.ord.ter., \quad (13)$$

where $\overline{[OH_v]} = \varepsilon \gamma_v \overline{T}^{-2.4}\overline{[O]} \cdot \overline{[M]}$, $[OH_v]'_M = \varepsilon \gamma_v \overline{T}^{-2.4}\overline{[O]}[M]'$, $[OH_v]'_O = \varepsilon \gamma_v \overline{T}^{-2.4}[O]'\overline{[M]}$, $[OH_v]'_T = -2.4\varepsilon \gamma_v T'\overline{T}^{-3.4}\overline{[O]} \cdot \overline{[M]}$, $[OH_v]''_{OM} = \varepsilon \gamma_v \overline{T}^{-2.4}[O]'[M]'$, $[OH_v]''_{TM} = -2.4\varepsilon \gamma_v T'\overline{T}^{-3.4}\overline{[O]}[M]'$, $[OH_v]''_{TO} = -2.4\varepsilon \gamma_v T'\overline{T}^{-3.4}[O]'\overline{[M]}$.

Hence, relative variations (RV) of emissions due to variations in temperature, [O], and concentration of air are:

$$RV'_T = 100\% \cdot \frac{[OH_v]'_T}{\overline{[OH_v]}} = 100\% \cdot -2.4\frac{T'}{\overline{T}},$$

$$RV'_O = 100\% \cdot \frac{[OH_v]'_O}{\overline{[OH_v]}} = 100\% \cdot \frac{[O]'}{\overline{[O]}}, \quad (14)$$

$$RV'_M = 100\% \cdot \frac{[OH_v]'_M}{\overline{[OH_v]}} = 100\% \cdot \frac{[M]'}{\overline{[M]}}.$$

The relative variations of concentrations due to second momenta are

$$RV''_{TM} = 100\% \cdot \frac{[OH_v]''_{TM}}{\overline{[OH_v]}} = 100\% \cdot -2.4\frac{T'[M]'}{\overline{T}\,\overline{[M]}},$$

$$RV''_{OM} = 100\% \cdot \frac{[OH_v]''_{OM}}{\overline{[OH_v]}} = 100\% \cdot \frac{[O]'[M]'}{\overline{[O]}\,\overline{[M]}}, \quad (15)$$

$$RV''_{TO} = 100\% \cdot \frac{[OH_v]''_{TO}}{\overline{[OH_v]}} = 100\% \cdot -2.4\frac{T'[O]'}{\overline{T}\,\overline{[O]}}.$$

In the decompositions (14) and (15), it was implicitly assumed that the variation of height of the OH* layer does not exceed scale height (when we decompose the air number density). Hence, these equations are valid for assessment of different impacts in [OH*] (volume emission) only for intervals where height deviations of OH* layer from averaged height are weak.

Calculations and Discussion:

The theoretical solutions derived above assume for quenching and spontaneous emission processes multi-quantum relaxation, at which transitions occur from all vibrational levels above to all levels below. To date, not all multi-quantum quenching coefficients for CO_2 and N_2 are known. Currently known are the so-called collisional cascade quenching rates, when for all vibrational levels transitions are assumed to one level below. Last update of these coefficients was presented by Krasnopolsky (2013) and Makhlouf et al. (1995) for quenching by CO_2 and N_2, respectively. We adopted these values, i.e. for $A_{vv'}$ and $G_{vv'}$ and use a diagonal matrix with values of Krasnopolsky (2013) and Makhlouf et al. (1995) for transitions $v \rightarrow v-1$ and assign the non-diagonal terms to zero.

The input profiles, were taken from the MCD

(Mars Climate Database), which is based on simulations with the Laboratoire de Météorologie Dynamique General Circulation Model (Forget et al., 1999). The MCD contains distributions of minor gases in the Martian atmosphere, including O_3 (Lefèvre et al., 2004; 2008), that is directly involved in OH^* production, H_2O (Navarro et al., 2014), which is the principal source of odd-hydrogens, and variations of other long-lived species (CO_2, N_2) involved in quenching processes (Forget et al., 1998, 2008).
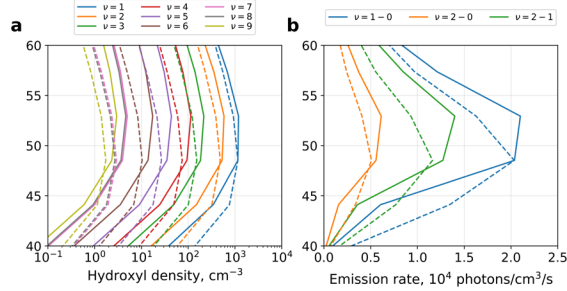
Figure 1. Nighttime averaged zonal mean, averaged over 70°N – 90°N, and L_s 265°-320° (in order to obtain colocation with Clancy et al. (2013) observations): (a) $OH_{v=1,...9}$, calculated by Eq. (1) (solid lines) and calculated by Eq. (7) (dashed lines), (b) volume emission calculated by Eq. (1) and (7) (solid and dashed lines, respectively) for vibrational transitions 1-0 (blue), 2-1 (green), and 2-0 (red).

Figure 1a illustrates a good agreement between $[OH^*]$ and peak altitudes calculated with the full model (Eq. 1) and with the simplified formula (Eq. 7). The best agreement occurs near the peaks at ~48-53 km. We explain differences below and above the peaks by deviations of O_3 from photochemical equilibrium in the polar night area, where O_3 lifetime is prolonged under the condition of permanent night and downward transport of O. Although for the modelling is better to use the full model (Eq. 1), nevertheless Eq. (7) is useful for qualitative analysis.

For Earth OH^* layer, a vertical separation OH^* by vibrational numbers (e.g. Adler-Golden, 1997) is well known. It cannot be explained from equation (9) (p does not depend on v). This is because we omitted quenching by O in the loss term for OH^*. Including this term into consideration (not shown here) results in a week vertical separation by vibrational numbers. Vertical distance between layers with different vibrational numbers is expected to be weaker than on Earth (as was found by Clancy et al. (2013)). This is because for Earth`s mesopause OH^* layer, O quenching, which is responsible for separation, is comparable with O_2 one, but for the Martian atmosphere it has negligible importance compared to CO_2 quenching.

Fig. 1b shows peaks at ~48-53 km and corresponding volume emissions in a good agreement with the Clancy et al. (2013) observations.

Equations derived above provide some predictions and can be applied for analysis, which we illustrate below.
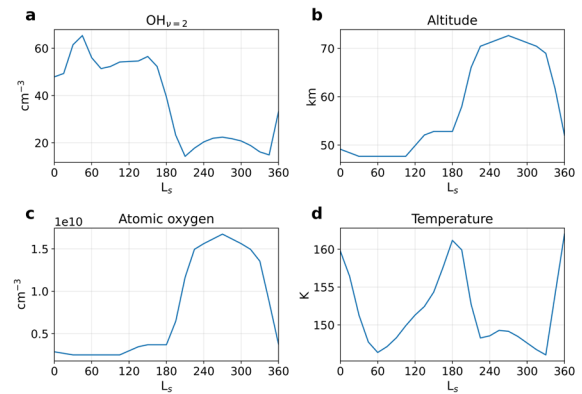
Figure 2. Nighttime mean one month sliding averaged values at peak of the $OH_{v=2}$ layer calculated by Eq. (1) at middle (40°N) latitudes: a) $[OH_{v=2}]$, b) height of peak, c) [O], and d) temperature.

The terrestrial OH^* airglow layer demonstrates annual and semiannual variations (e.g., Gao et al., 2010). Similar variations can be expected from the Martian OH^* due to seasonal changes in [O], air number density and temperature. Fig. 2 shows time series of nighttime one-month sliding averaged values at the peak of the $OH_{v=2}$ layer calculated with (1) at middle (40°N) latitudes: a) $[OH_{v=2}]$, b) the height of the peak, c) [O], and d) temperature. It is seen that the concentration and the height of the peak at the northern middle latitude vary seasonally with the maxim concentrations and lowest height occurring during the first half of the year (L_s=0°-180°). The amplitude of the annual height variation on Mars is more than 20 km (Fig. 2b), which by several times exceeds that near the Earth mesopause (~5-10 km). The figures show a clear anticorrelation between the $[OH_{v=2}]$ and the height of the peak, as also follows from (8). Since volume emission is linearly proportional to the $[OH^*]$, this points out to an anticorrelation between the emission and the height of the layer. A similar anticorrelation has also been observed on Earth (e.g., Gao et al., 2010).

Fig. 2a and 2c demonstrate a correlation between [O] and $[OH^*]$. This correlation happens between L_s~210° and 340°, where the minor maximum of $[OH^*]$ coincides with the maximum of [O]. The correlation between the air density and the peak altitude is even more robust, because the magnitude of seasonal variations of the air density is larger than [O]. The effects of O and air densities on the OH^* layer oppose each other. When the OH^* layer is low at summer, the air density is large, while the [O] is small. The OH^* layer moves higher at winter, the air density decreases, but the [O] rises. In Earth`s mesosphere at high and middle latitudes, the behavior of the OH^* layer is opposite: high altitude and low emission at summer, but lower altitude and stronger emission at winter. This is because the main driver for OH^* layer on Earth is O, which is transported downward in winter and upward in summer. On Mars, the layer behavior is determined additionally by air density variations. Seasonal changes of tem-

perature play a minor role in the annual cycle of OH^*, since it varies only by about 15 K over the year (Fig. 2d).

In order to illustrate an assessment of the inputs into OH^* layer variability from different sources, we calculate relative variations due to [O], temperature, and concentration of air at 40°N. For our analyses we use first half of the year (L_s=0°-180°) when deviations of OH^* height from semi-annual averaged height do not exceed the scale height (≈10 km). For this example the overbar in Eq. (14) and Eq. (15) denotes semi-annually averaged values and prime denotes difference of actual (modeled) values from averaged.
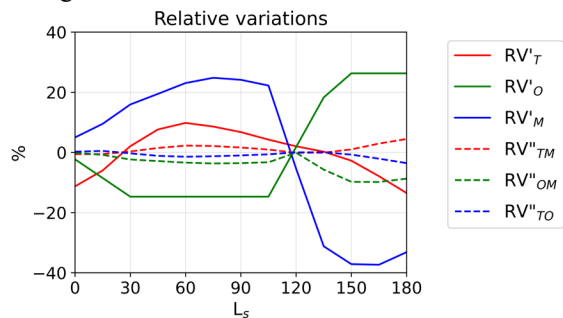
Figure 3. Relative variations calculated by Eq. 14 (solid lines) and Eq. 15 (dashed lines) at 40°N, for first half of the year.

Fig. 3 shows decomposition of OH^* variation by Eq. (14) and Eq. (15) as solid and dashed lines, respectively. The variations of temperature (red lines) play a minor role, whereas variations due to O and air concentrations are of the same order (variation due to air number density is slightly larger) with action in antiphase. The first peak of OH^* at L_s~40°-50° (Fig. 2a) is determined primarily by growth of air number density (blue line) and secondary due to temperature decline (Fig. 2d and red line on Fig. 3). The secondary peak of [OH^*] at L_s~150° (Fig. 2a) is primarily determined by growth of [O] (green line) when declining air concentration and growing temperature act in opposite direction. The variations due to 2nd momenta are weaker and they do not exceed 10%.

Summary and Conclusions:

The simplified relations for OH^* in the Martian atmosphere at nighttime conditions for height of OH^* peak and concentration at peak were derived with assumptions that: 1) total quenching by CO_2, O_2, and N_2 dominate over quenching by O and spontaneous emission; 2) O_3 is in photochemical equilibrium in the vicinity of OH^* layer. Under these approximations, nighttime [OH^*] at peak is proportional to the [O] and negative power of temperature. The [OH^*] in the vicinity OH^* layer is directly proportional to the pressure (i.e., inversely to the layer altitude). Hence OH^* emission, which comes almost from the vicinity of the peak, anticorrelates with the height of the OH^* layer. OH^* layer on Mars may reveal annual and

semi-annual cycles, as the result of annual (semi-annual) cycles of temperature, air concentration, [O], and their superpositions. The expressions for assessment of relative variation of OH^* due to variations of temperature, [O], and concentration of air were obtained. All these expressions can be useful for analysis and interpretation of hydroxyl emission observations. Eqs. (9) and (10) gives possibility to infer altitude of OH^* peak and [O] at OH^* peak by surface based airglow observations.

References:

Adler-Golden, S. (1997), J. Geophys. Res., 102, 19969–19976, doi:10.1029/97JA01622.

Burkholder, J. B., et al. (2020), JPL Publication 19-5, http://jpldataeval.jpl.nasa.gov.

Caridade, P. J. S. B., Horta, J.-Z. J., Varandas, A. J. C. (2013), Atmos. Chem. Phys., 13, 1-13, doi:10.5194/acp-13-1-2013.

Clancy, R. T., et al., (2013), Icarus, 226, 272-281, doi:10.1016/j.icarus.2013.05.035.

Forget, F., Hourdin, F., Talagrand, O. (1998), Icarus, 131, 302-316, doi:10.1006/icar.1997.5874.

Forget, F., et al. (1999), J. Geophys. Res., 104, 24155-24176, doi:10.1029/1999JE001025.

Forget, F., Millour, E., Montabone, L., Lefevre, F. (2008), 1447, 9106, Bibcode:2008LPICo1447.9106F.

Gao, H., Xu, J., Wu, Q. (2010), J. Geophys. Res. 115, A06313, doi:10.1029/2009JA014641.

García-Muñoz, A., McConnell, J. C., McDade, I. C., Melo, S. M. L. (2005), Icarus, 176, 75–95, doi:10.1016/j.icarus.2005.01.006.

González-Galindo, F., et al. (2013), J. Geophys. Res., 118, 2105-2123, doi:10.1002/jgre.20150.

González-Galindo, F., et al (2015), J. Geophys. Res., 120, 2020-2035, doi:10.1002/2015JE004925.

Krasnopolsky V. A. (2006), Icarus, 185, 153–170, doi:10.1016/j.icarus.2006.06.003.

Krasnopolsky V. A. (2010), Icarus, 207, 638–647, doi:10.1016/j.icarus.2009.12.036.

Krasnopolsky V. A. (2013), Planet Space Sci., 85, 78–88, doi:10.1016/j.pss.2013.05.022.

Krasnopolsky, V. A. and Lefèvre, F. (2013), Comparative Climatology of Terrestrial Planets, Univ. of Arizona, 231–275, doi:10.2458/azu_uapress-9780816530595-ch11.

Lefèvre, F., Lebonnois, S., Montmessin, F., Forget, F. (2004), J. Geophys. Res., 109, E07004, doi:10.1029/2004JE002268.

Lefèvre, F., et al. (2008), Nature, 454, 971-975, doi:10.1038/nature07116.

Makhlouf, U. B., Picard, R. H., Winick, J. R. (1995), J. Geophys. Res., 100, 1128911311, doi:1029/94JD03327.

Navarro, T., et al. (2014), J. Geophys. Res., 119, 1479-1495, doi:10.1002/2013JE004550.

Xu, J., Gao, H., Smith, A. K., Zhu, Y. (2012), J. Geophys. Res., 117, D02301, doi:10.1029/2011JD016342.